ON THE INCREASE OF INTRINSIC WORKABILITY AND HOT WORKING TEMPERATURE RANGE OF M42 LEDEBURITIC SUPER HIGH SPEED STEEL IN AS-CAST AND WROUGHT STATES

D. Bombač[1, a], M. Tercelj[2], M. Fazarinc[2] and G. Kugler[2]

[1]University of Cambridge, Department of Materials Science and Metallurgy, 27 Charles Babbage Road, Cambridge CB3 0FS, UK
[2]University of Ljubljana, Faculty of Natural Sciences and Engineering, Aškerčeva 12, 1000 Ljubljana, SI-Slovenia

Keywords: AISI M42, soaking, hot workability, carbides, precipitation

Abstract
In order to remain competitive to powder metallurgy and spray forming, further improvements of a classical production route are needed and desired. This paper describes the means by which the intrinsic hot deformability may be improved and the temperature range of the safe hot working extended for AISI M42 super high speed steel, one of the most challenging materials with respect to hot deformability. A special hot compression procedure is described to determine appropriate soaking temperatures of as-cast and semi-wrought states. Moreover, conventional hot compression tests in the extended temperature range (850 °C - 1150 °C) and strain rates range 0.001 – 5 s^{-1} were carried out. The complex behaviour of carbides is discussed, which depends on the soaking temperature and time, deformation temperature and strain rate. Deformation conditions for improved crushing of initial eutectic carbides networks during the first stages of hot working are identified. Apparent activation energies for hot working in two temperature ranges and constants of the hyperbolic sine function are determined. The microstructure and respective carbides are characterised by field emission scanning electron microscope, optical microscopy, X-ray diffraction and the results compared to equilibrium thermodynamic calculations using ThermoCalc.

1. Introduction

High speed steels (HSS) are commonly ledeburitic tool steels which are alloyed with carbide forming elements (Cr, W, Mo, V) to achievethe required strength, hardness, toughness, ductility, fatigue resistance, and other properties required for cutting tools [1-2]. Solidification of ledeburitic tool steels ends by a eutectic transformation of the residual interdendritic liquid to austenite and various carbides formed in a typical networked structure. These carbides are known as eutectic cells or eutectic carbides. Beside eutectics, primary (precipitated before the eutectic transformation) and secondary carbides are present too. The characteristics of carbides, i.e. morphology, shape and size, amount, distribution, etc., are decisive in the resulting HSS properties, i.e. mechanical and manufacturing (workability) properties, and need to be considered during steel processing. HSS are predominately produced by the classical route of ingot casting followed by hot forging, rolling and subsequent heat treatments. In order to remain competitive compared to powder metallurgy and spray forming processing routes, further improvements of this classical production route are needed and in much demand [3-13].

[a] Corresponding author: David Bombac, University of Cambridge, email: db513@cam.ac.uk

During steel processing (heating, hot deformation and cooling), carbides formed undergo various transformations from decomposition, dissolution, crushing due to deformation, precipitation, growth and coarsening. Characteristics of carbides depends on the processing parameters (casting temperature, solidification rate, soaking temperature and time, deformation conditions) and steel initial chemical composition [6,10,14-33]. Carbide properties and their transformations influence carbide characteristics and significantly impact hot workability of steel through stress state and deformation parameters. Reduced hot workability of HSS refers to the narrowed range of lower and upper limits of the safe hot working temperature range and the reduced general intrinsic workability in the medium temperature range. The upper limit is related to the growth of grains and carbides, the occurrence of incipient melting of eutectic carbides and eutectic phases with a low melting point. The lower limit of the safe hot working range is related to the precipitation of secondary carbides, their characteristics in the matrix and/or on grain boundaries and a diminished rate of recrystallisation. Slight variations of processing parameters and chemical composition can have significant influence on carbide characteristics and consequently on the intrinsic hot workability of steel and the variability of the resulting properties. However, different HSS's exhibit different combinations of influences which points to very complex behaviours of carbides on the intrinsic hot workability for each individual processing condition [17, 33-43]. In order to increase the intrinsic hot workability, not only of individual HSS compositions, but individual states obtained during HSS processing, needs to be assessed. Furthermore, since the characteristics of carbides depends on temperature, it is very important to determine the influence of soaking temperature on the shift in the lower and upper limits of the safe working temperature ranges and its general effect on intrinsic hot workability. Studies related to processing parameters, characteristics of carbides and hot workability of HSS are scarce [33, 38] as each HSS has specific parameters related to hot workability. This makes studies of particular HSS and microstructural states on intrinsic hot workability of great appeal.

AISI M42 super high speed steel (SHSS) is a premium cobalt-containing high speed steel with a chemical composition designed for high hardness and superior hot hardness. Its chemical composition, beside increased contents of Co (more than 8 wt %) and Mo (more than 9 wt %) has significant amounts of Cr, W and V. Content of these elements is considerably higher compared to the ordinary HSS's and indicates difficult and significantly decreased hot workability in comparison to the ordinary HSS's. This makes AISI M42 SHSS one of the lowest hot workable HSS's, a problem so far not solved sufficiently.

The aim of this study is to increase the intrinsic hot workability, extend the temperature range of safe hot working and to determine the optimal soaking conditions for AISI M42 SHSS. The study was conducted by employing thermo-mechanical simulations for various types of hot compression tests in over a wide range of temperature and strain rate for as-cast and semi-wrought microstructures. Optical and electron microscopy combined with X-ray diffraction (XRD) are used to study carbide transformations. The study revealed optimal hot deformation conditions leading to improved crushing efficiency of initial eutectic carbide network cells during the first stages of hot deformation. For the as-cast and semi-wrought microstructural states, apparent activation energies for hot deformation and the corresponding hyperbolic sine equation constants are determined. The authors believe that the aim to increase intrinsic hot workability and to extend the temperature range of safe hot working was achieved and should improve yield during steel manufacturing not only for AISI M42, but also for other similar SHSS.

2. Experimental methods

2.1 Material and hot deformation procedure

The chemical composition of the studied AISI M42 SHSS is given in **Table 1**. The steel was prepared in an electric arc furnace, deoxidised in a vacuum furnace and cast into a 500 kg ingot, referred from here on as the as-cast state. The as-cast ingot was soft annealed and forged into a billet with diameter of 103 mm and is referred from here on as being in the semi-wrought state. Cylindrical specimens for thermo-mechanical studies were machined from both states, with a diameter of 10 mm and length of 15 mm.

Table 1. Chemical composition of studied AISI M42 SHSS in wt %.

C	Si	Mn	Cr	Mo	V	W	Co	Fe
1,11	0,24	0,27	3,84	9.35	1.12	1,38	8.24	Balance

The optimal soaking temperature and hot deformation parameters were studied with a thermo-mechanical simulator Gleeble 1500D in an Ar atmosphere to prevent oxidation. The optimal soaking temperature or upper temperature limit of safe hot working was determined by soaking specimens for 2 h followed by compression at the soaking temperature up to the true strain values of 0.7 and 0.9, with a constant strain rate of 1 s^{-1}, for the as-cast and semi-wrought samples, respectively. The upper safe hot working temperature is determined as the highest temperature where macro cracks on the surface of deformed specimens were not observed. The optimal lower safe hot working temperature was determined by soaking specimens first on the optimal soaking temperature, followed by cooling to a deformation temperature (initially at 900 °C, as this is the lowest industrially accepted deformation temperature for this type of steel) and compression up to true strains of 0.7 and 0.9, with constant strain rate of 1 s^{-1}, for the as-cast and semi-wrought microstructures, respectively. This procedure was iterated with decreasing deformation temperature in 10 °C steps until cracks were observed on the deformed sample surface. The lower safe hot working temperature is considered the last deformation temperature without any observed surface cracks on the sample.

The identified safe hot deformation temperature limits were subsequently used to study hot workability of M42 SHSS. Cylindrical samples were heated with a heating rate of 4 °Cs^{-1} to the optimal soaking temperature and held there for 600 s and then cooled with a cooling rate of 6 °Cs^{-1} to the deformation temperature where they were held for an additional 600 s prior to deformation. The obtained appropriate soaking temperature enables safe hot deformation in the temperature ranges of 850 °C to 1130 °C for the as-cast and 850 °C to 1150 °C for the semi-wrought states. Thermo-mechanical simulations were conducted for a range of strain rates between 0.001 s^{-1} and 5.0 s^{-1}. To avoid inhomogeneous deformation, Ta foils, 0.05 mm in thickness, and graphite foils were inserted between the cylindrical specimen and the compression tool. The obtained microstructure of hot deformed samples was retained by water quenching immediately after deformation. True stress vs. true strain curves were calculated, taking into account heat generated due to high strain rates and the temperature increase was compensated by using the method described by Liu et al. [40].

2.2 Characterization of microstructure

Metallographic samples were cut along the mid plane and prepared using conventional grinding and polishing steps and etched at room temperature in Methanol Regia for 5-10 s before conducting optical microscopy (OM) using a Leica DM2500 M light microscope and electron microscopy using a FEI Nova NanoSEM 450 scanning electron microscope (SEM) in combination with attached energy dispersive X-ray spectroscopy (EDX) for observation of

microstructure and chemical mapping of carbides. Electron backscatter diffraction (EBSD) measurements were taken with a Bruker e⁻Flash^{1000} detector.
Conventional X-ray diffraction (XRD) measurements were performed on polished samples to confirm the presence of the phases using a Bruker D8 Advance X-ray diffractometer with position sensitive detector (LynxEye EX) and Cu-Kα radiation (λ = 1.5406 Å). A continuous scanning mode was chosen with a rate of 0.02°/s over an angular width of 2θ = 30-120 °. A Ni filter was used to obtain a nearly monochromatic X-ray beam. XRD was performed on several of the samples with several microstructural states and deformation conditions, the details of such are given in **Table 2**.

Table 2: Microstructure and deformation conditions of for XRD

Sample	Microstructure and deformation temperature
1	As-cast
2	Semi-wrought
3	As-cast deformed and at 1130 °C
4	As-cast deformed and at 850 °C
5	Semi-wrought and deformed at 1150 °C
6	Semi-wrought and deformed at 850 °C

3. Results and discussion

3.1 Thermodynamic equilibrium calculations

To begin with, in **Fig. 1** we show an overview of the expected phases, their amounts, and the temperature ranges as obtained from equilibrium thermodynamics using Thermo-Calc 2015b with the TCFE8 database. Equilibrium phases were calculated with the chemical composition given in **Table 1** in the temperature range of 500 °C to 1500 °C.

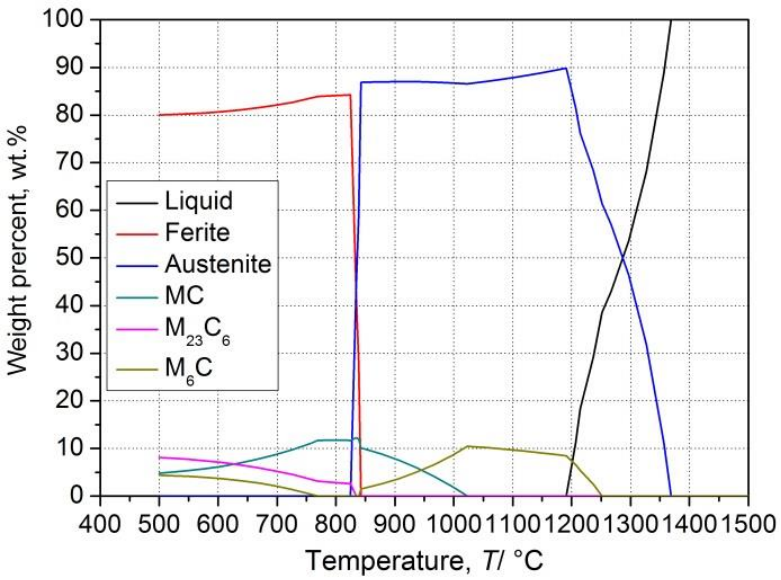

Figure 1: Equilibrium predicted by Thermo-Calc for AISI M42 HSS.

A stability phase diagram shows the start of austenite formation at 1365 °C from the liquid, followed by precipitation of primary M_6C carbides at 1250 °C. According to literature (cf.

references [6,10,16-18,24,29,31-32]), primary M_6C carbides are expected to precipitate on the austenite grain boundaries. Solidification is completed at 1190 °C and the volume percent of M_6C carbide increases upon cooling to 1025 °C at the expense of austenite. Below 1025 °C, M_6C carbides start to transform to MC carbide and a eutectoid reaction takes place in the temperature range between 840 °C and 825 °C, where austenite transforms to ferrite and M_6C carbides fully dissolve. During the same time as ferrite grows, the MC carbide volume percent increases and then starts to decrease as $M_{23}C_6$ carbides start to precipitate. M_6C carbides start to form again below 760 °C. At the expense of the MC volume fraction, the amount of $M_{23}C_6$ and M_6C carbides increases.

3.2 XRD analysis of both initial microstructures and hot deformed samples

The phases observed in the thermodynamic equilibrium simulations give us a good first approximation. However, processed materials can result in microstructures considerably different to those observed by thermodynamic equilibrium simulations. The as-cast state should be closest to equilibrium due to the slow cooling of the ingot. To get a better picture of the phases present in the studied material, XRD was performed. The results presented are for all states (ct. **Table 2**) compounded and depicted in **Fig. 2** and discussed in light of thermodynamic equilibria and subsequent microscopy analysis. It is emphasised that only the relevant peaks, i.e. for carbides (M_xC_y) and α-Fe (Fe) are marked.

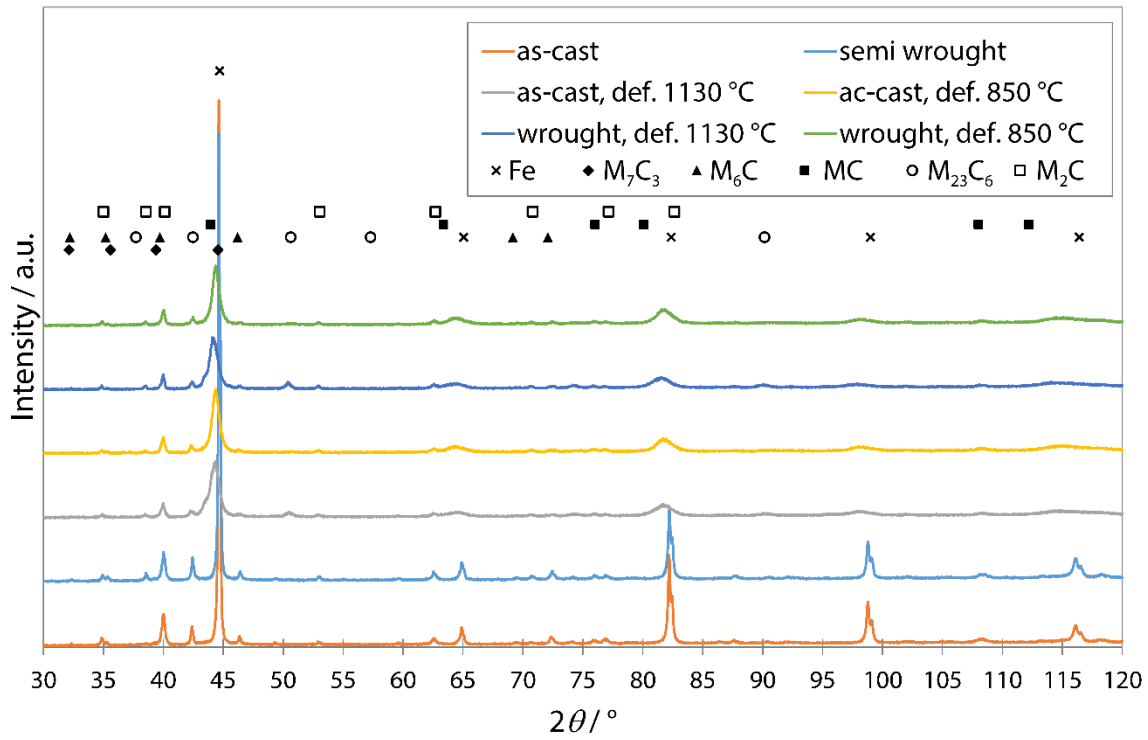

Figure 2: X-ray diffraction patterns for all deformation states with marked main carbides and α-Fe peaks for as-cast microstructure.

Phase identification using only XRD is extremely difficult as most peaks overlap and increased 2θ angle scans need to be made. The as-cast microstructure was identified as a mixture of martensite, ferrite, retained austenite and several types of carbides. Carbides detected in the as-cast state sample were hexagonal Mo based M_2C, cubic W and Fe based M_6C and cubic Cr based $M_{23}C_6$ and possibly miniscule amounts of hexagonal M_7C_3. In the

semi-wrought sample, we identified the presence of similar types of carbides with slightly higher amounts of secondary M_7C_3 carbide due to the long soaking of the ingot before and during the deformation steps. Since these microstructures were obtained from an industrial process, peaks for Fe are sharp due to the controlled cooling after casting or initial hot deformation. Other samples were deformed using a thermo-mechanical simulator where the microstructure was frozen by immediate water quenching after deformation. The Fe peaks show some broadening, suggesting large amounts of retained austenite (2θ at approximately 45°) and high amounts of C in the martensite. Due to the large retained strains in quenched samples, peaks are shifted to the left, indicating a smaller lattice parameter size. The M_7C_3 carbide was not detected in the water quenched samples (samples 3-6 in **Table 2**). This was attributed to soaking (2 h) not being sufficiently long to transform it into the more stable M_6C carbide. A similar observation can be made for M_2C carbide too, which was found in larger quantities (from corresponding peak intensities) in the industrially processed microstructure, i.e. sample 2, during soaking and deformation in the laboratory environment causing its transformation into the more stable M_6C and MC carbides. The obtained results for the as-cast state are in agreement with results obtained in [29], however with an additional presence of the $M_{23}C_6$ carbide. The MC, M_7C_3, $M_{23}C_6$ and smaller sized M_6C carbides are most likely secondary carbides, precipitated and transformed in the solid state.

3.3 As-cast and semi-wrought microstructures

As-cast and semi-wrought microstructures of studied AISI M42 SHSS are shown in **Fig. 3** and **Fig. 4**, respectively. Both microstructures are at first described and then discussed in light of obtained XRD results and thermodynamic equilibrium calculations.

3.2.1 As- cast microstructure

A micrograph of the as-cast state is shown in **Fig. 3a**, with a higher magnification image of eutectic carbides in **Figs. 3b**. **Fig. 3c presents a** backscatter electron micrograph, and EDS chemical distribution maps for Mo, W and Cr in **Figs. 3d-3f**. The microstructure is composed of martensite, retained austenite, spheroidised eutectic carbides, very fine lamellar eutectic carbides and fine secondary carbides in the matrix. Electron backscatter diffraction (EBSD) revealed that spheroidised primary eutectic carbides with micrometre size and fine lamellar eutectic carbides are M_2C carbides. This is in agreement with literature [6,10,29-33] for as-cast microstructures of ledeburitic tool steels. Comparison of **Fig. 3c** and **Figs. 3d-3f** confirms that M_2C eutectic carbides are mainly composed from Mo (cf. **Fig. 3d**) with smaller amounts of W (cf. **Fig. 3e**) and Cr (cf. **Fig. 3f**). Since V exhibited a similar chemical distribution as shown for W in **Fig. 3e,** it is not displayed. The Map for Cr (cf. **Fig. 3f**) indicates a wider distribution area compared to the eutectic carbide network (cf. **Fig. 3c**) and is at some sections very dense, indicating secondary chromium based carbides, confirming XRD results (presence of $M_{23}C_6$ and M_7C_3). A similar observation holds also for W and is attributed to secondary carbides. EBSD was used to analyse secondary carbides in the matrix. A micrograph with marked carbides is shown in **Fig. 3g**, from which the following is determined: carbide marked by "1" was determined to be M_2C (Mo based), carbide 2 as M_6C (Fe_3W_3C) and carbide 3 as Cr_7C_3 with its Kikuchi pattern given in **Fig. 3f**. Comparing identified carbides with XRD and from microscopy for the as-cast microstructure we confirmed the presence of Mo_2C, Cr_7C_3, Fe_3W_3C, V based MC and $Cr_{23}C_6$ carbides. Larger eutectic and primary carbides are mainly M_2C carbides with M=Mo, W, V and M_6C carbides with M=W, Fe; while amounts of MC and $Cr_{23}C_6$ are tiny.

The chemical composition of carbides was additionally confirmed with EDS. Spots analysed are shown in the backscatter electron micrograph of **Figure 4**, while EDS results are given in **Table 3.** Spots 1, 3 and 5 were taken on carbide lamellae with a relative high width (approximately 4 – 7 μm). The main carbide forming elements were detected: Mo is in the range 46-56%, W 7.2 –8.5%, V 5.3 – 6.9% and Cr 5.1 – 6.3%. Fe was detected in the range of 4.8 – 18.2% and exhibits inverse correlation with Mo and Co content below 2% in carbides. Additionally C was analysed, although EDS tends to overestimate its content (C was detected in the range of 16.3 – 21.5%). Spots 2 and 4 were taken in the matrix, where spot 2 is further away from carbides than spot 4. The matrix exhibits large amounts of Fe and Co in the range close to the initial chemical composition, confirming that Co is not a carbide forming element, but serves to retain mechanical properties of the matrix at high temperature.

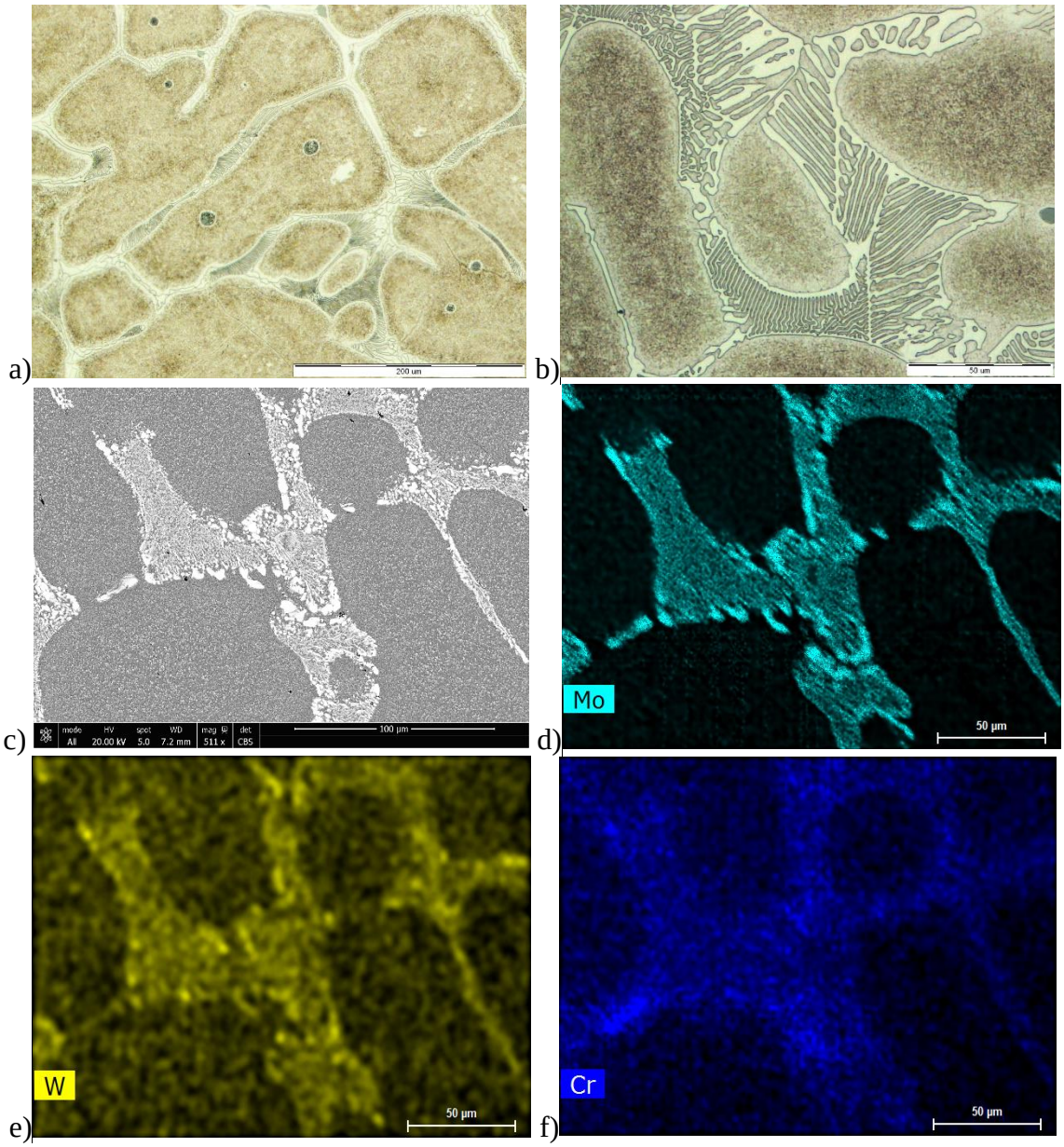

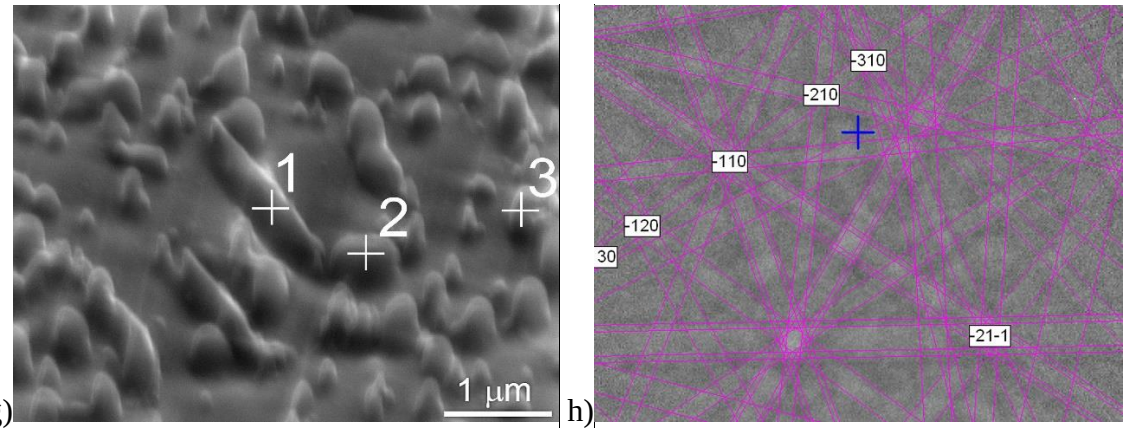

g) h)

Figure 3: As-cast (ingot) microstructure of M42 SHSS; a) optical micrograph , b) detail of eutectic carbides, c) backscatter electron micrograph, d) Mo distribution map, e) W distribution map, f) Cr distribution map, g) distribution of sub micrometre carbides in matrix and h) Kikuchi pattern of M_7C_3 carbide (spot 3 in subfigure g).

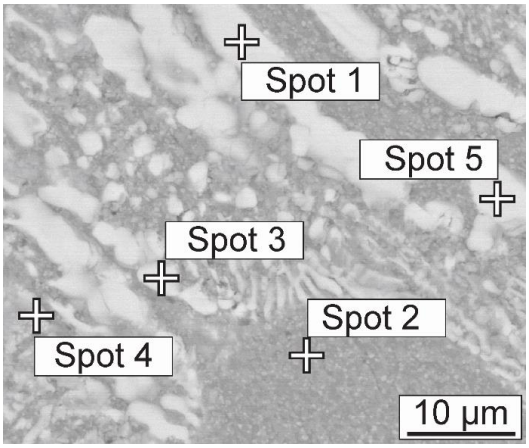

Figure 4: Backscatter electron micrograph with marked spots for EDS analysis.

Table 3: Chemical composition from EDS of marked spots in **Figure 4**.

Spot in **Figure 4**	Content / wt%						
	C	V	Cr	Fe	Co	Mo	W
1	21.5	6.1	6.3	6.3	0.5	52.2	7.2
2	8.7	0.5	2.6	74.9	9.3	3.1	1.0
3	16.3	5.3	6.0	18.2	1.9	46.3	7.1
4	12.9	2.4	3.8	51.3	6.0	20.3	3.4
5	17.8	6.9	5.9	4.8	0.4	55.7	8.5

3.2.2 Semi-wroughtmicrostructure

The microstructure of the semi-wrought billet forged from the as-cast ingot is shown in **Figure 5a** and exhibits a smaller grain size and spheroidised carbides with at least two distinct carbides structures, judging from the OM contrast. A backscatter electron micrograph taken at higher magnification is given in **Figure 5b**, marked with spots where EDX spectra were collected. Results from EDX are given in **Table 4**. The carbide network structure, typical for the as-cast microstructure, was crushed and it almost entirely disappeared with carbides coagulated and transformed into spheres. Slight remains of initial carbide networks

can be seen, with lamellar eutectic carbides in proximity of grain boundaries. The size of the largest carbides is approximately 8-10 μm. Carbides with size exceeding 3 μm, marked as 1, 2, 3, 5 and 6 in **Figure 5b** are formed through coalescence of crushed initial carbide networks and primary carbides. The main chemical element detected is Mo, with weight percent in the range from 36 wt% to 52 wt%, W in the range 6.6 wt% to 9.8 wt% and, V and Cr with content below 7.7 wt% and 5.7 wt%, respectively. With confidence, we can state that unstable M_2C carbide, manly composed with Mo, V, W and Cr (cf. **Figures 3c-f**) transformed into M_6C carbide type during soaking and the deformation process. EDX revealed the presence of Mo, V and W, while Cr content is much lower compared to the content in the eutectic carbides (cf. **Table 3**). The transformation of eutectic carbides follows; M_2C + matrix → M_6C + MC or M_2C + γ-Fe → MC + M_7C_3+ M_6C [6, 10, 16-18,24,29,31-32]. EDX elemental mapping of the wrought microstructure showed that carbides with a size exceeding 3 μm mainly contain Mo (**Figure 5c**), V (with similar chemical distribution compared to Mo) and W (**Figure 5d**), with distribution of the latter not limited only to larger carbides. More uniform distribution of W throughout the matrix points to small M_6C carbides, most likely secondary carbides. Carbide at the spot 7 and with size below 3 μm has an increased content of Mo and is M_2C, whilst the carbide at the spot 8 is most likely M_6C.

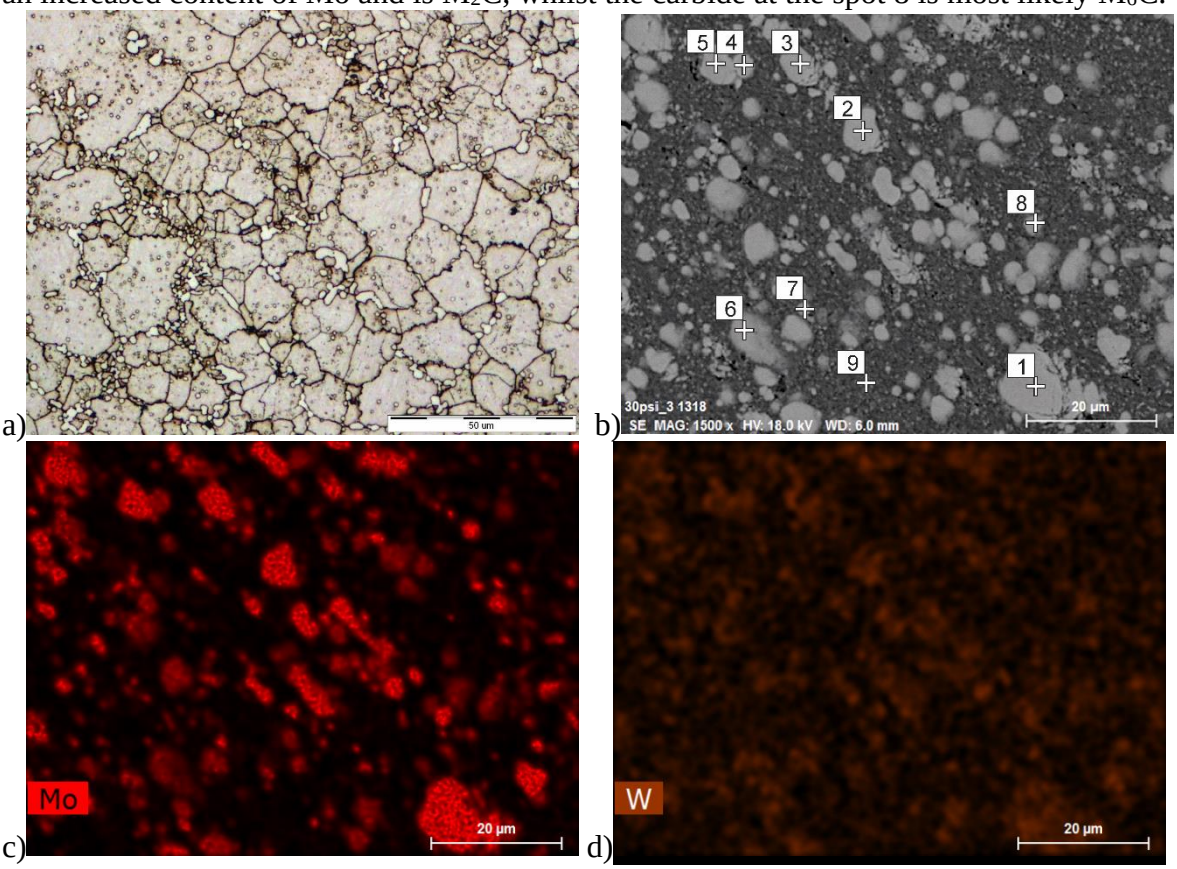

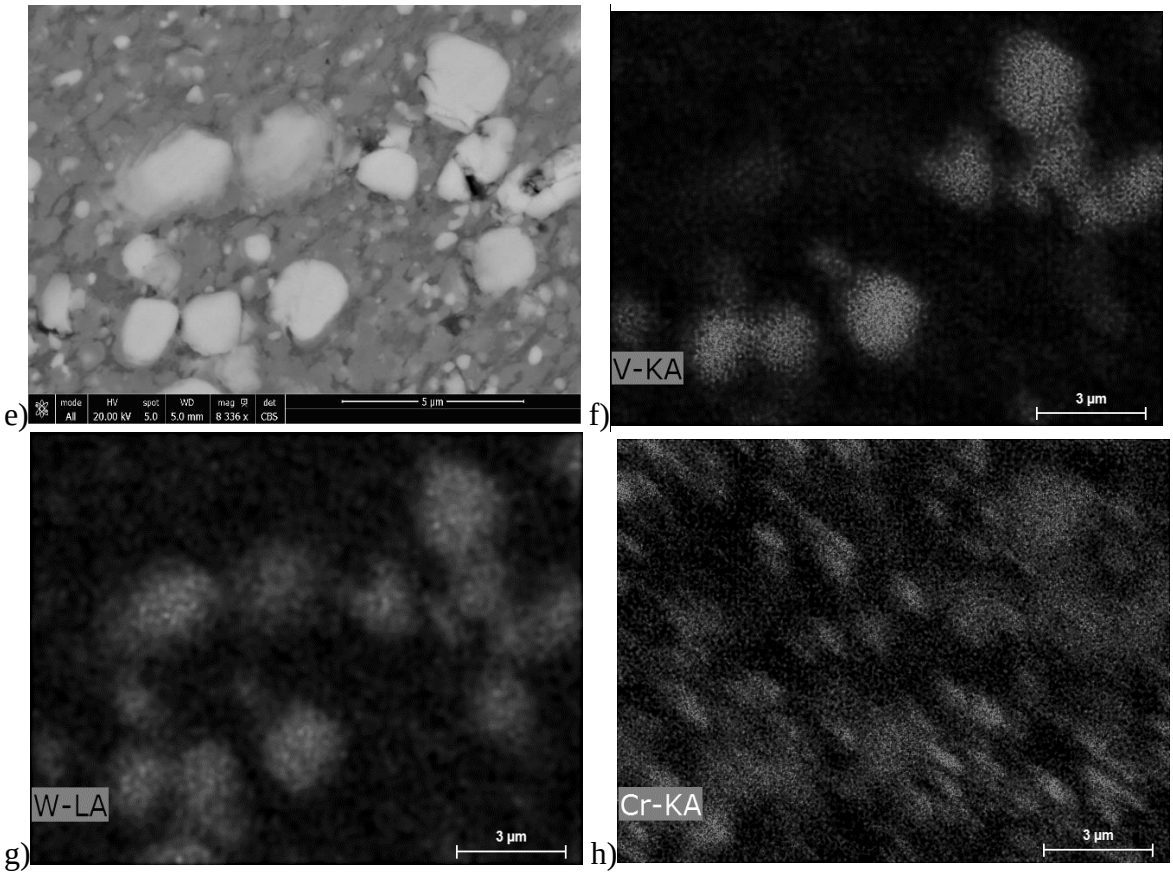

Figure 5 Micrograph of the semi-wrought (billet forged to diameter of 103 mm); a) microstructure from OM, b) BSE image with points where EDX spectra was taken, c) elemental distribution of Mo, d) elemental distribution of W, e) BSE image with higher magnification, f) elemental distribution at higher magnification of V, g) elemental distribution of W, and h) elemental distribution of Cr.

Table 4: EDX quantitative results from spots marked in **Figure 5b**, where 2 size classes are marked as L for carbides larger than 3 µm and S for smaller carbides.

Spot in	Content / wt%							Size
Figure 5b	C	V	Cr	Fe	Co	Mo	W	class
1	20.4	7.7	5.7	4.5	-	52.9	8.8	L
2	21.1	6.1	5.3	9.1	-	49.0	9.5	L
3	20.8	6.3	5.7	4.9	0.5	52.0	9.8	L
4	17.2	1.6	2.8	29.3	3.9	36.2	9.0	S
5	21.1	7.9	5.3	4.9	0.3	51.4	9.2	L
6	17.1	1.4	2.8	36.0	4.6	30.4	7.8	L
7	19.6	7.5	5.0	10.3	1.2	47.0	9.5	S
8	15.7	1.0	2.7	44.5	5.4	23.8	6.6	S
9	12.4	0.5	3.1	72.7	8.8	2.3	0.2	S

L - large sized carbides
S - small sized carbides

In **Figure 5e,** a backscatter electron micrograph taken at higher magnification with smaller (below 3µm) carbides is shown. Elemental distribution maps corresponding to **Figure 5e** are presented for V, W and Cr in **Figures 5f**, **5g** and **5h**, respectively. The distribution of Cr is present thorough the area pointing to the tiny secondary carbides, while the distribution of W and V is limited to spherical carbides with a size larger than 1 µm. From the difference in

both distribution maps we can identify two carbide types, also confirmed by the different contrast in **Figure 5e**. There is an interesting interplay between V and Fe, where Fe is detected in the carbides, with a reduced content of V, confirming M_6C to be Fe_3W_3C. The Carbide richer in V is most likely of MC type and Cr rich carbides - M_7C_3 and $M_{23}C_6$ in agreement with XRD results.

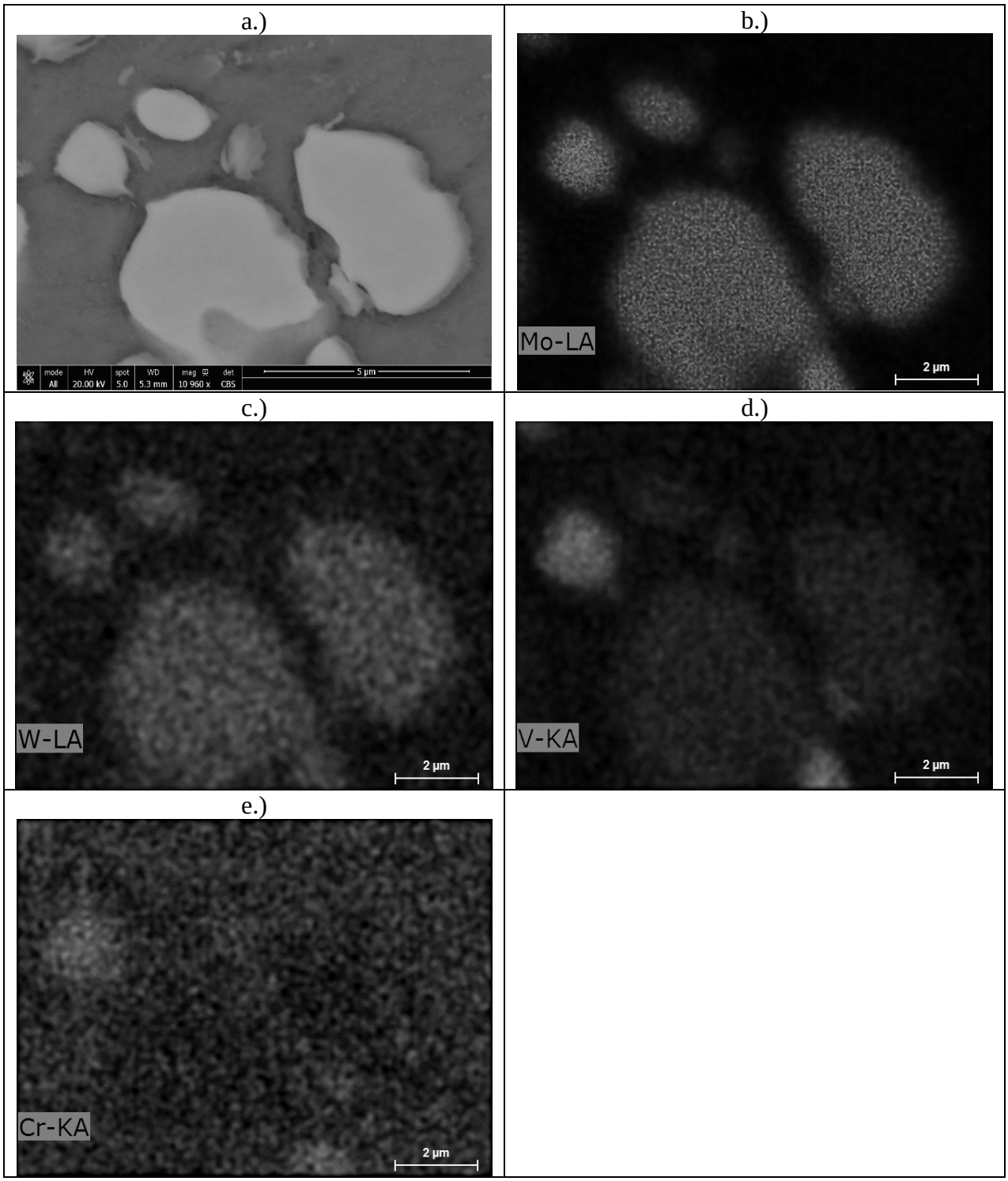

Figure 6: Size of carbides in deformed samples at 850 °C and $1s^{-1}$ (a), distribution (mapping) of Mo in carbides (b), distribution of W (c) and distribution of V in carbides (d).

In **Figure 6,** a BSE micrograph and elemental distribution maps of the samples deformed at temperature of 850 °C and strain rate $1s^{-1}$ are depicted. Using EBSD, it was confirmed that carbides are M_6C composed mostly of Mo and W. However, carbides rich in V are of MC type. Elemental distributions are shown in **Figures 6b**, **6c** and **6d** for Mo, W and V, respectively. The Distribution of Cr shown in **Figure 6e** exhibits a more uniform distribution throughout the matrix, pointing to secondary M_7C_3 carbides, and increased V content in MC carbide.

3.4 Optimal soaking temperature

To determine the optimal soaking temperature, a special procedure for hot compression was developed, with details published elsewhere [37]. In this case, the optimal soaking temperature was determined after soaking for 120 min followed by hot compression up to strains of 0.7 for the as-cast microstructure and 0.9 for the semi-wrought microstructure. An optimal temperature was selected as temperature where cracks did not occur on the deformed samples' surface.

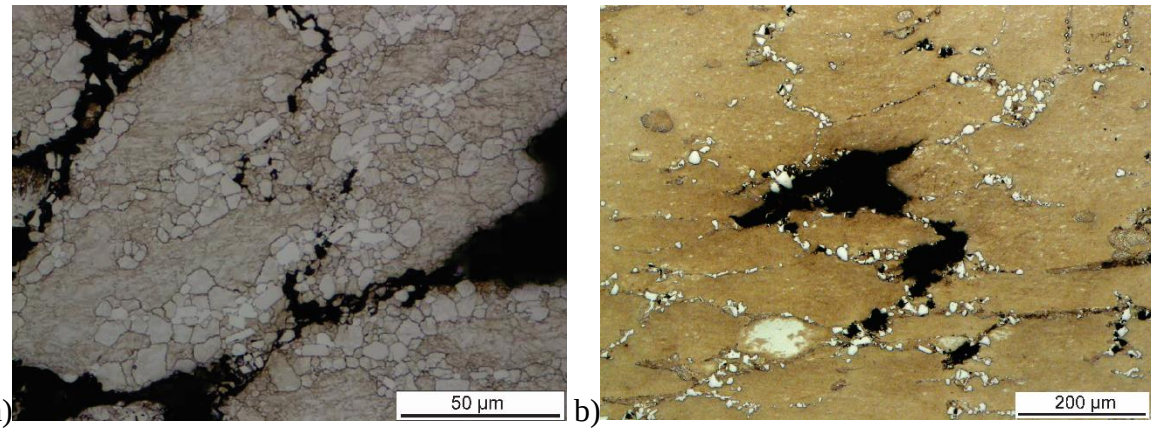

Figure 7 Occurrence of cracking on grain boundaries on as-cast microstructure soaked at 1170 °C for 120 minutes and deformed: at 1170 °C (a) and at 850 °C (b), strain rate $1s^{-1}$.

Higher soaking temperatures cause extensive carbide growth leading to cracks at both the higher soaking temperature (1180 °C) and the lower limit of the safe hot working window (850 °C). In **Figure 7a,** cracks occurred after soaking at 1170 °C followed by deformation at the same temperature are shown. This soaking temperature is considerably higher than the upper temperature limit of the safe hot working range. In **Figure 7b,** cracks occurred after soaking at 1170 °C for 120 min, followed by deformation at 850 °C (around the lower limit of the safe hot working temperature window). From **Figure 7** it can be seen that cracks are predominantly at grain boundaries, indicating a clear connection to increased carbides size. The solution is to lower the soaking temperature and thus decrease the growth of carbides during soaking. The optimal soaking temperatures were determined as 1130 °C for the as-cast microstructure and 1150 °C for the wrought microstructure. These temperatures were also selected as an upper limit of the safe hot working temperature and no cracking appeared until hot compression at 850 °C which is the lower limit of the safe hot working window. The obtained optimal soaking temperatures are approximately 40 °C lower than the eutectic temperatures obtained using differential thermal analysis (DTA). Furthermore, DTA showed that at temperatures above 1150 °C, melting of ledeburitic eutectic takes place, which results in a local as-cast secondary microstructure during cooling to the deformation temperature. Soaking of the as-cast microstructure at 1180 °C resulted in a slightly reduced higher

temperature limit of safe hot working, 1120 °C, and an increased lower temperature limit of safe hot working, to approximately 900 °C. Moreover, optimal soaking temperatures determined in the present work do not result in extensive carbide growth.
Our results point to a reduced temperature window of safe hot working if the chosen soaking temperature is too high, due to the increased growth of carbides.

3.5 Single hit stress-strain curves and development of microstructure

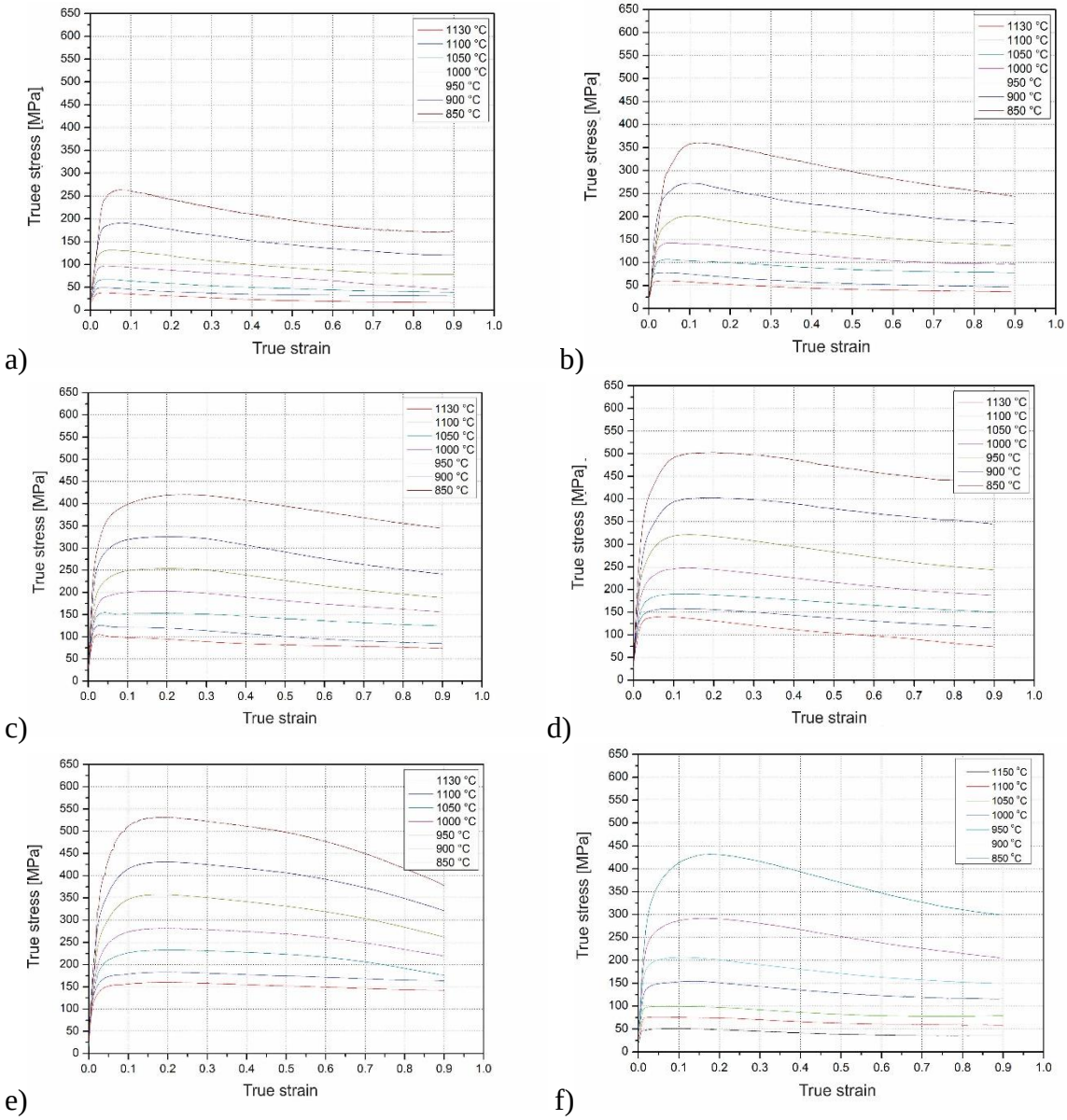

Figure 8 Stress-strain curves collected at different strain rates and temperatures, i.e. for strain rate of 0.001 s^{-1} (a), 0.01 s^{-1} (b), strain rate 0.1 s^{-1} (c), strain rate 1s^{-1} (d), strain rate 5 s^{-1} (e) for as-cast state and for strain rate 0.01 s^{-1} for wrought state (f).

Typical single hit stress-strain curves (several tests were conducted for each set of conditions) are presented in this section. **Figure 8** illustrates the effect of temperature and strain rate on stress-strain curves for the as-cast microstructure (**Figures 8a-e**). Flow curves were obtained in the temperature range between 850 °C and 1130 °C at strain rates from 0.001 s^{-1} to 5 s^{-1}. In **Figure 8f**, the temperature effect at a strain rate of 0.01 s^{-1} for the wrought microstructure

is shown. All flow curves displayed a rapid initial increase to a stress maximum, characterised by a peak stress and strain, followed by a decrease in flow stress, due to lower effective stress to move dislocations and increased softening as effect of recrystallisation. Compression between flow response of the as-cast and wrought microstructures show approximately 10 % higher stresses for the wrought microstructure. A variety of different factors can be contributed to this, e.g. smaller grain size, increased number density of carbides, etc. which all result in increased flow stresses. A Significant contribution towards the increase of stress at the same strain is a mechanical dispersion of carbides in the matrix, which act as pinning particles during grain growth and strengthen the matrix as can be seen in the micrographs depicted in **Figure 9**. Peak flow stress values are shifted to larger strains with increased strain rate or decreased deformation temperature, implying dynamic recrystallisation during hot deformation.

The microstructural evolution as a function of strain rate at a deformation temperature of 1130 °C in the middle of the compression is shown in **Figure 9**. The microstructure of the as-cast specimen at strain rates of 1 s^{-1} and 5 s^{-1}, even at a strain of 0.7, still contains traces of as-cast microstructure where the eutectic carbide network is not fully crushed. Moreover, differences in carbide distributions in the matrix can be seen and are attributed to dynamic recrystallisation. For example, compression with a strain rate of 5 s^{-1} does not allow enough time for recrystallisation or to influence the distribution of a broken eutectic network more uniformly through the matrix (**Figure 9b**). More uniform carbide distribution in the matrix is visible in **Figure 9a** where compression with strain rate of 1 s^{-1} allows sufficient time for recrystallisation and formed a more uniform microstructure with smaller grain size. The most uniform carbide distribution in the matrix was achieved with the lowest strain rate (0.001 s^{-1}), the microstructure of which is shown in **Figure 9c**. This observation explains why initial stages of hot deformation of the as-cast microstructure have significant effects on yield during hot working. From the obtained results it follows that initial deformation of the as-cast microstructures should be performed with a reduced strain rate. In industrial deformation, the best results would be obtained by prior ingot forging with lower strain rates and subsequent hot rolling where strain rates are usually higher than 1 s^{-1}, making hot rolling less appropriate for initial ingot deformation. Similar differences in microstructural uniformity are seen for deformation performed at temperature of 1050 °C, shown in **Figures 9d** and **9e,** and deformation performed at temperature of 850 °C, shown in **Figures 9f** and **9g,** for strain rates 1 s^{-1} and 5 s^{-1}, respectively. Clear carbide size differences can be seen in developed microstructures obtained using strain rates 1 s^{-1} and 5 s^{-1} at all temperatures, whereas with lower strain rates, smaller carbide sizes are obtained.

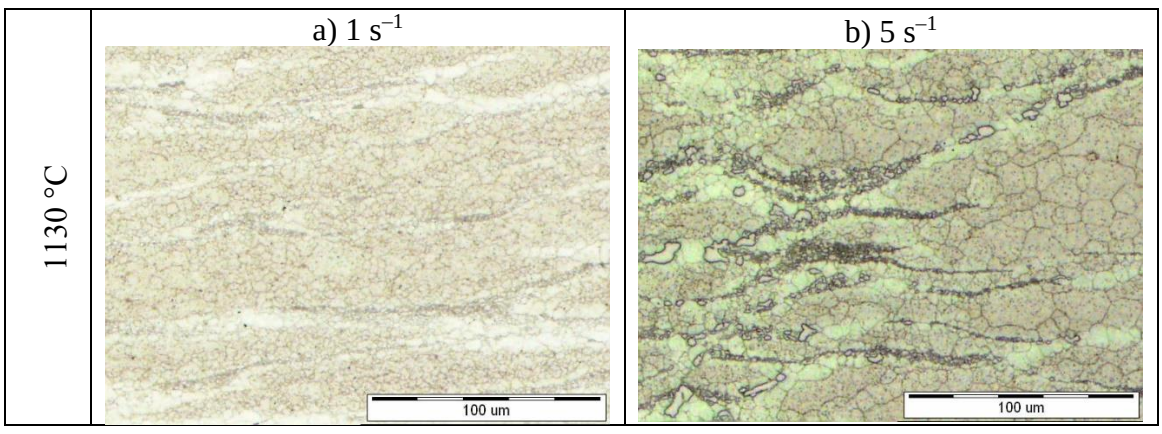

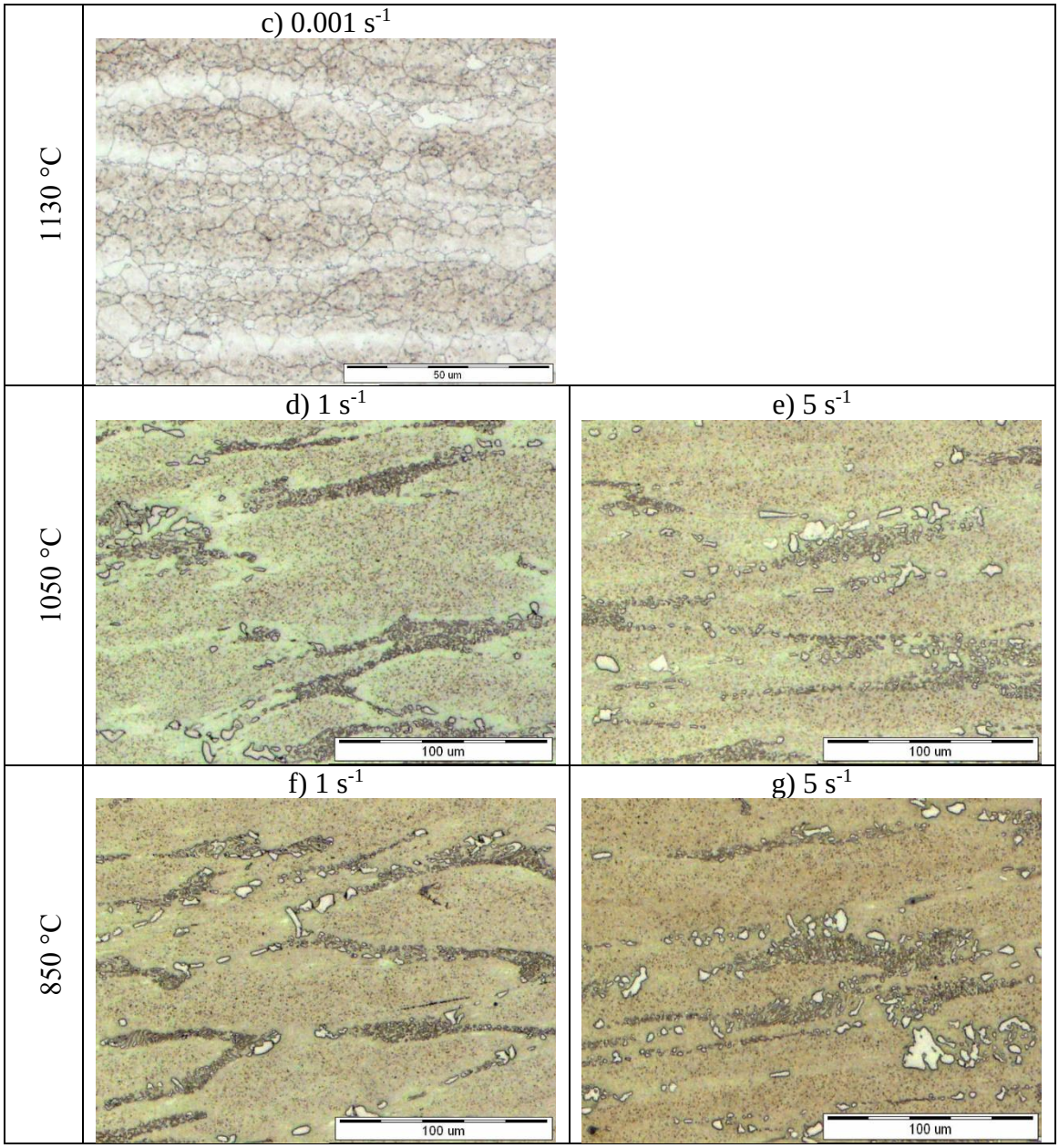

Figure 9: Microstructures of deformed samples for as-cast state of M42 HSS for different temperatures and strain rates: for 1130 °C for strain rate of $1s^{-1}$ (a), for $5s^{-1}$ (b) and $0.001s^{-1}$ (c), for 1050 °C and 1 s^{-1} (d) and for 5 s^{-1} (e), and for 850 °C and 1 s^{-1} (f) and for 5 s^{-1} (g).

The developed microstructures of semi-wrought samples, deformed at a temperature of 1150 °C are depicted in **Figures 10a** and **10b** for strain rates 1 s^{-1} and 5 s^{-1}, respectively. It can be seen that a smaller grain size was obtained using the higher strain rate. Similar behaviour was observed at all temperatures with exception of deformation at a temperature of 850 °C where carbide size and distribution and grain sizes were comparable as shown in **Figures 10c** and **10d**. Deformation at the lower limit of the safe hot deformation exhibits coalescence of carbides, with the largest carbide with 5-6 μm in diameter and grain size from a few and up to 15 μm. These observations imply that a wrought billet should be deformed with a higher strain rate, whereas laboratory hot deformation tests showed more uniformly developed microstructure.

Using the laboratory determined temperature window of safe hot working and optimal soaking temperature, an industrial hot working run was performed. An as-cast ingot was initially forged to a round billet with a diameter of 103 mm and then hot rolled to a final round bar of diameter 18 mm. The microstructure at the end of the industrial rolled bar is shown in **Figure 10e**, where grains size is comparable to that simulated in laboratory, while carbide size is slightly larger at 7-8 μm. This size increase was attributed to coalescence and coarsening and precipitation of secondary carbides. Furthermore, crushed and spheroidised eutectic carbides are visible at the grain boundaries and precipitated secondary carbides inside grains. It can be seen that using the optimal soaking temperature for the as-cast and semi-wrought states does not lead to an increased grain sizes, and obtained carbides coarsen, which exhibits good mechanical properties for the final tools.

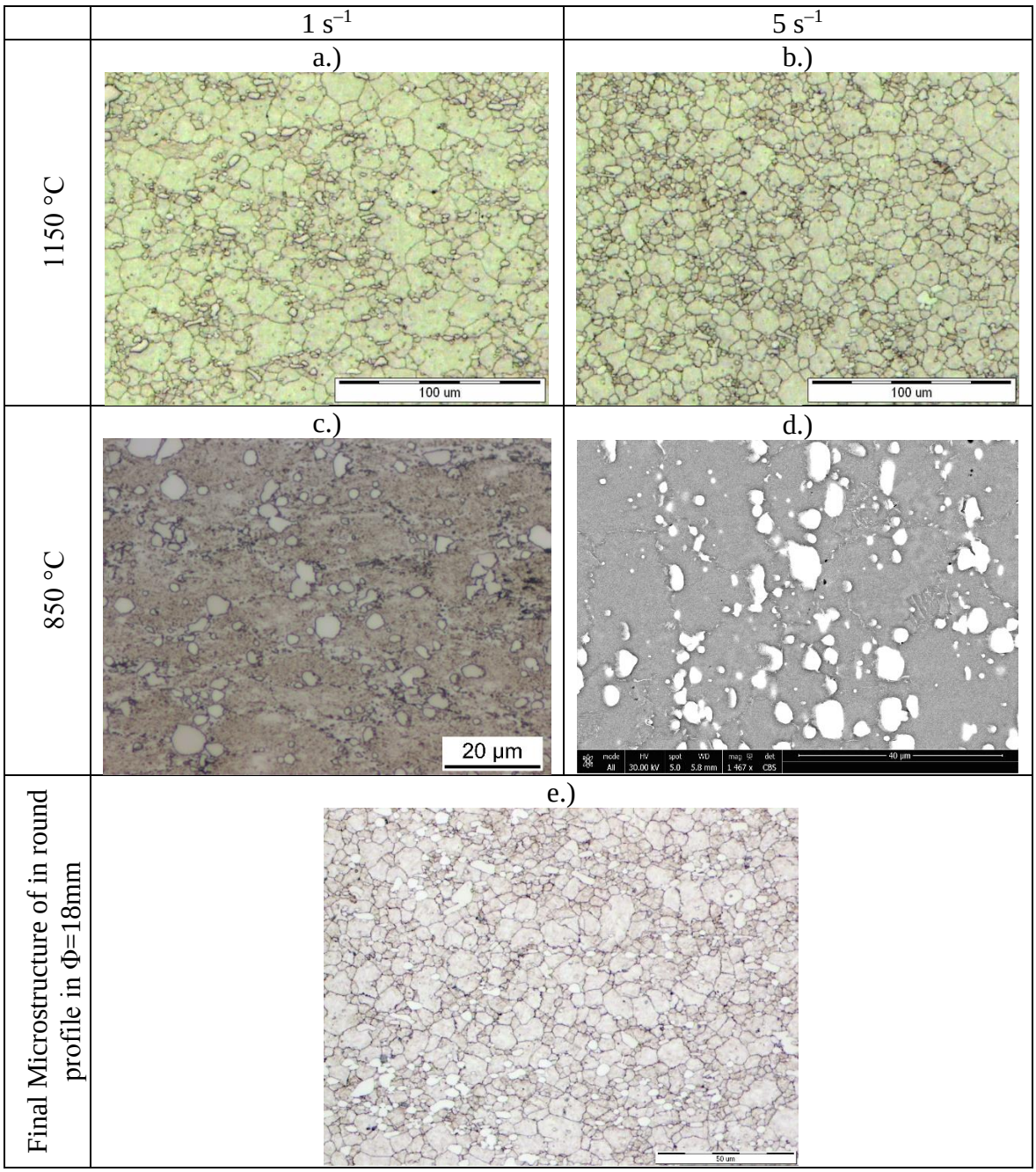

Figure 10: Microstructures of deformed samples for semi-wrought state: at 1150 °C for strain rate of $1s^{-1}$ (a) and for $5s^{-1}$ (b), at 850 °C for 1 s^{-1} (c) and for 5 s^{-1} (d) and final microstructure of hot rolled round profile of Φ=18 mm (e).

3.5 Stress- strain relationship

Values for the peak stresses for as-cast and wrought specimens from single hit hot compression tests and for all deformation conditions were collected and plotted in **Figure 11a** and **11b**, respectively. There is a clear decaying trend of peak stress with increased temperature. As expected, peak stress values augment with increasing strain rate at any given temperature. The activation energy for hot deformation can be derived using the following Zener–Hollomon parameter and hyperbolic sine equation [44];

$$Z = \dot{\varepsilon}\exp(\frac{Q}{RT}) = A(\sinh \alpha\sigma)^n \quad (1)$$

where Z is the Zener-Hollomon parameter, R is the gas constant, Q is the apparent activation energy for hot deformation, and A, n and α are constants. The details of the minimisation procedure and determination of parameters are given elsewhere [45, 46].

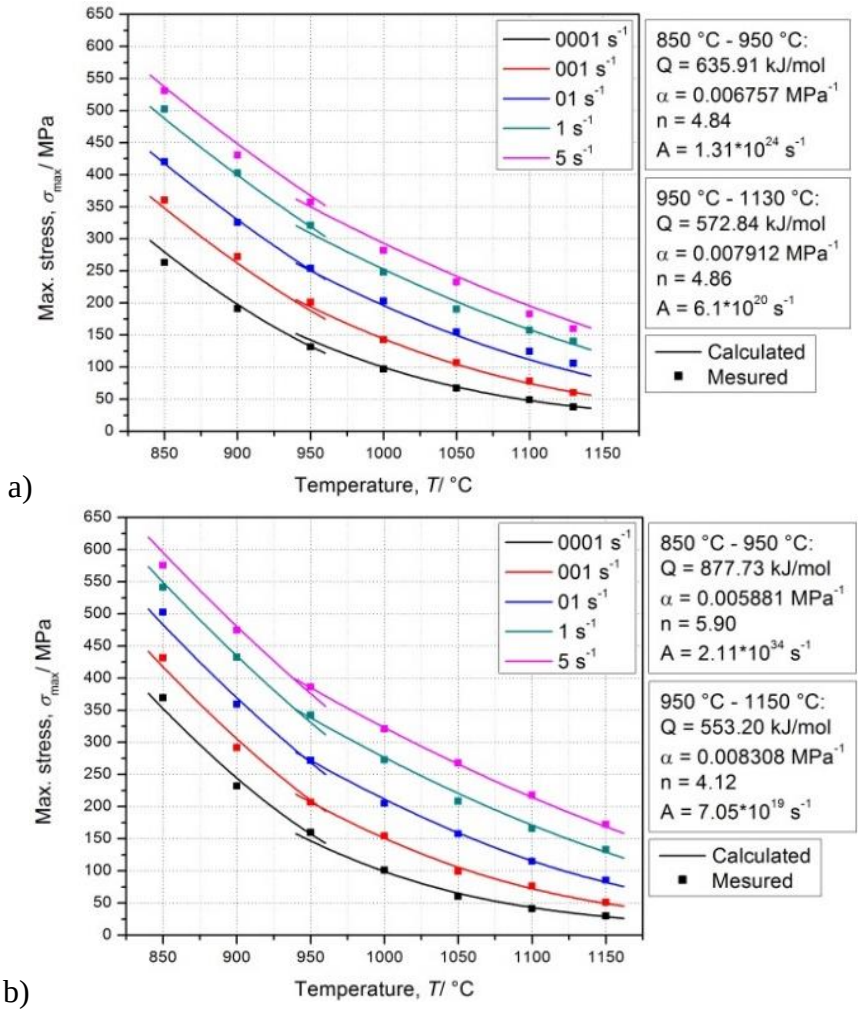

Figure 11 Single hit hot compression peak stresses vs. temperature and strain rate for; a) as-cast starting microstructure and b) wrought starting microstructure.

The calculated values for apparent activation energy for deformation are collected in Table 5 with results from literature for similar steels.

The peak stress and temperature relation described by a hyperbolic sine function using equation (1) are, along with experimental data, depicted in **Figure 11** for two temperature ranges. The first temperature window is between 850 °C and 950 °C, and the second temperature window is between 950 °C and 1130 °C or 1150 °C, depending on the sample's starting microstructure. Good agreement between experimentally and analytically obtained results is shown. Justification for two distinct temperature windows where different hyperbolic sine parameters are used stem from the fact that increased precipitation of secondary carbides below 1000 °C takes place.

Table 5: Comparison between the obtained values for apparent activation energies of hot working for various tool steels found in the literature with obtained values in our investigation.

Steel	Microstructure	Q / kJmol^{-1}	Temperature range / ºC	Strain rate range / s^{-1}	Ref.
M42	As-cast	572.8	950 - 1130	0.001-5	Present study
		635.9	850-950		
	Wrought	553.2	950 - 1150		
		877.7	850 - 950		
1.17C-11.3Cr-1.48V-2.24W-1.35Mo	Wrought	554	950-1150	0.001-6	[37]
		1125	850-950	0.001-0.1	
		1039	850-950	0.1-6	
T1	Wrought	654	950-1000	0.001-10	[40]
		467	1000-1150	0.001-10	
M2	As-cast	608	900-1000	0.18-3.63	[41]
		422	1000-1100	0.18-3.63	
		877.7	850 - 950		

Our study yields similar values of the apparent activation energies for deformation for the as-cast state (572.84 kJmol^{-1}) and wrought state (553.20 kJmol^{-1}) in the temperature windows 950-1130 ºC and 950-1150 ºC, respectively and is comparable to the values for similar steels from literature [37,40,41]. However, the apparent activation energies for deformation in the lower temperature deformation window are significantly different, and this was attributed to the precipitation of secondary carbides. Other hyperbolic sine parameters (cf. **Figures 11**) are in good agreement with literature, where the determined hardening exponent n is between 2 and 6, [17-24]. Our study revealed almost the same values of hardening exponent for the as-cast microstructure for both deformation temperature windows. The hardening exponent for the wrought microstructure increases from 4.2 to 5.9 in the upper deformation temperature window due to precipitation of secondary carbides as discussed previously, where equilibrium thermodynamics calculation predicts precipitation of MC carbides below 1040 °C.

4. Conclusions

Equilibrium thermodynamic calculations in combination with XRD were used to characterise M42 high speed tool steel. Carbide evolution during hot deformation was elucidated with help of OM, SEM with EDX and EBSD and XRD. A thermo-mechanical simulator was used to determine optimal soaking and expand the temperature window for safe hot working, deformation conditions, and the relationship between stress, temperature and strain rate in order to increase the hot workability of M42 HSS. The obtained peak stresses at different temperatures and strain rates were used to model apparent activation energies for hot deformation. The following conclusions can be reached from the work:

- Equilibrium thermodynamic calculations predicted the presence of M_6C, MC and $M_{23}C_6$ carbides. XRD of the as-cast state, being closest to equilibrium, confirmed all predicted phases and also pointed to the presence of metastable M_2C, M_7C_3 carbides. EBSD was used to validate the structure of carbides and confirmed the presence of all mentioned types with exception of $M_{23}C_6$ type. MC, $M_{23}C_6$ and M_7C_3 types refer to secondary carbides.
- XRD of the semi-wrought microstructure pointed to the presence of M_2C M_6C, MC, M_7C_3 and $M_{23}C_6$.
- The determined optimal soaking temperatures for the as-cast and wrought microstructures are 1130 °C and 1150 °C, respectively.
- The determined temperature window of hot working is between 850 and 1130 °C for the as-cast microstructure, and between 850 °C and 1150 °C for the wrought microstructure. Following this determined temperature window, it is clear that an improvement in intrinsic hot workability is possible.
- In order to increase hot deformation yield, any initial eutectic carbide network in the as-cast microstructure must be crushed during the first stages of hot working. As this can be achieved with lower strain rate during deformation, it is our recommendation to use a strain rate of $1 s^{-1}$, which is acceptable for industrial processing. Conversely, for the semi-wrought microstructure, higher strain rates are recommended, as smaller grain sizes were obtained in samples deformed at higher strain rates.
- The apparent activation energies for hot deformation were calculated for two temperature ranges. The higher temperature range, between 950 °C and 1130 °C (1150°C for the wrought microstructure) yields activation energies of 572.84 kJ mol^{-1} and 553.20 kJ mol^{-1} for the as-cast and wrought states, respectively. The lower temperature range, between 850 °C and 950 °C, yields activation energies of 635.91 kJ mol^{-1} and 877.73 kJ mol^{-1} for the as-cast and wrought states, respectively. Constitutive equations which describe flow stress as a function of strain rate and deformation temperature are:
    - $\dot{\varepsilon} = 6.1x10^{20}(\sinh 0.00791\sigma)^{4.84} \exp(572.8/RT)$ {as-cast, 950 - 1130°C}
    - $\dot{\varepsilon} = 1.31x10^{24}(\sinh 0.00676\sigma)^{4.86} \exp(635.9/RT)$ {as-cast, 850 - 950°C}
    - $\dot{\varepsilon} = 7.05x10^{19}(\sinh 0.00831\sigma)^{4.12} \exp(553.1/RT)$ {wrought, 950 - 1150°C}
    - $\dot{\varepsilon} = 2.11x10^{34}(\sinh 0.00588\sigma)^{5.90} \exp(877.7/RT)$ {wrought, 850 - 950°C}.
- The calculated peak stresses are in good agreement with experiments.
- The use of the determined optimal soaking temperature resulted in the maximum carbide size of 5-6 μm during hot deformation at 850 °C. Employing this optimal soaking temperature for an industrially rolled bar to produce a final diameter of 18 mm resulted in carbides of approximately 7-8 μm, and a grain size of 15 μm,

indicating that good mechanical properties should be acquired in final products made from such a bar.

Acknowledgements

We thank Dr Miles A. Stopher for his help and discussions. This work was supported by the Slovenian Research Agency (ARRS) under programme grants P2-0344 and P2-0268.

References

[1] G. Roberts, G. Krauss, R. Kennedy, Tool Steels, 5th Edition, (AMS International, 1998).
[2] H. Brandis, E. Haberling, H. H. Weigard, Processing and Properties of High Speed Tool Steels, (M.G.H. Wells and L.W. Lherbier, Ed., TMS_AIME, 1980), 1-18.
[3] Faraz Deirmina, Massimo Pellizzari and Matteo Federici, Production of a Powder Metallurgical Hot Work Tool Steel with Harmonic Structure by Mechanical Milling and Spark Plasma Sintering, Metallurgical and Materials Transactions A, 48 (2017), 1910.
[4] C. Rodenburg, W.M. Rainforth, A quantitative analysis of the influence of carbides size distributions on wear behaviour of high-speed steel in dry rolling/sliding contact, Acta Materialia 55 (2007) 2443–2454.
[5] D.H. Hetzner, Refining carbide size distributions in M1 high speed steel by processing and alloying, Materials Characterisation, 46 (2001), 175-182.
[6] H. F. Fischmeister, R. Riedl, and S. Karagöz, Solidification of high speed tool steels, Metallurgical Transactions A, 20A (1989), 2133-2148.
[7] M. Boccalini, H. Goldenstein, Solidification of high speed steels, International Materials Review, 46/2 (2001), 92-115.
[8] M. R. Ghomashchi: Quantitative microstructural analysis of M2 grade high speed steel during high temperature treatment, Acta Materialia, 46/14 (1998) 5207 - 5220.
[9] Minwoo Kang, Young-Kook Lee, The Effects of Austenitizing Conditions on the Microstructure and Wear Resistance of a Centrifugally Cast High-Speed Steel Roll, Metallurgical and Materials Transactions A 47/7 (2016) 3365–3374.
[10] Eon-Sik Lee, Woo-Jin Park, J. Y. Jung, S. Ahn, Solidification microstructure and M_2C carbide decomposition in a spray-formed high-speed steel, Metallurgical and Materials Transactions A, 29/5 (1998) 1395–1404.
[11] F. Yana, H. Shi, B. Jin, J. Fan, Z. Xu, Microstructure evolution during hot rolling and heat treatment of the spray formed Vanadis 4 cold work steel, Materials Characterization, 59 (2008) 1007-1014.
[12] Chang Kyu Kim, Yong Chan Kim, Jong Il Park, Sunghak Lee, Nack J. Kim, Jung Seung Yang, Effects of alloying elements on microstructure, hardness, and fracture toughness of centrifugally cast high-speed steel rolls, Metallurgical and Materials Transactions A, 36/1 (2005) 87–97.
[13] J. Gontarev, M. Doberšek, J. Medved, P. Mrvar, Solidification of hipereutectoid high speed steel for rolls, Metalurgija, 50 (2011) 1, 29-32.
[14] S. Sackl, H. Leitner, H. Clemens, S. Primig, On the evolution of secondary hardening carbides during continuous versus isothermal heat treatment of high speed steel HS 6-5-2, Materials Characterization, 120 (2016) 323–330.

[15] Xue-Feng Zhou, Wang-Long Zhu, Hong-Bing Jiang, Fengfang, Yi−You Tu, Jian-Qing Jiang, A New Approach for Refining Carbide Dimensions in M42 Super Hard High-speed Steel, Journal of Iron and Steel Research International 23/8 (2016), 800-807.
[16] Ghomashchi, M. R. Quantitative microstructural analysis of M2 grade high speed steel during high temperature treatment. Acta Materialia, 46 (1998), 5207–5220.
[17] Zhou, B., Shen, Y., Chen, J. & Cui, Z. S. Breakdown Behavior of Eutectic Carbide in High Speed Steel During Hot Compression. Journal of Iron and Steel Research International 18, 41–48 (2011).
[18] Fu-Sheng Pan, Wei-Qing Wang, Ai-Tao Tang, Li-Zhi Wu, Ting-Ting Liu, Ren-Ju Cheng, Phase transformation refinement of coarse primary carbides in M2 high speed steel, Progress in Natural Sciences: Materials International, 21 (2011) 180–186.
[19] Fusheng Pan, Peidao Ding, Aitao Tang, Carbides in high-speed steels containing silicon, Metallurgical and Materials Transactions A, 35/9 (2004) 2757–2766
[20] H. Kim, J.Y. Kang, D. Son, T.H. Lee, K.M. Cho, Evolution of carbides in cold-work tool steels, Materials Characterization, 107 (2015) 376-385.
[21] D. Bombac, M. Fazarinc, A. Saha Podder, G. Kugler, Study of Carbide Evolution During Thermo-Mechanical Processing of AISI D2 Tool Steel, Journal of Materials Engineering and Performance 22 (2013) 742–747.
[22] Peidao Ding, Gonggqoi Shi, Shouze Zhou, As-cast Carbides in High-Speed Steels, Metallurgical Transactions A, 24 (1993) 1265-1271.
[23] Luan Y, Song N, Bai Y, Kang X, Li D, Effect of Solidification Rate on the Morphology and Distribution of Eutectic Carbides in Centrifugal Casting High-speed Steel Rolls, Journal of Materials Processing Technology, 210 (2010), 536-541.
[24] Xiaodan Zhang, Wei Liu, Dale Sun, Youguo Li, The Transformation of Carbides during Austenization and Its Effect on the Wear Resistance of High Speed Steel Rolls, Metallurgical and Materials Transactions A, 38/3, (2007) 499–505.
[25] Hongshuag Di, Xiaoming Zhang, Guodong Wang, Xianghua Liu, Spheroidizing kinetics of eutectic carbide in the twin roll-casting of M2 high-speed steel, Journal of Materials Processing Technology, 166 (2005), 359-363.
[26] Lei Chen, Jianming Pei Fei, Li Yingjie, Zhang Mingjia, Wang Xiaocong Ma, Decomposition Reaction of Metastable M2C Carbide in a Multi-Component Semi-High-Speed Steel, Metallurgical and Materials Transactions A 47/12 (2016) 5662–5669
[27] M. A. Hamidzadeh, Mahmood Meratian, A. Saatchi, Effect of cerium and lanthanum on the microstructure and mechanical properties of AISID2 tool steel, Materials Science & Engineering A 571 (2013) 193–198.
[28] Hebin Wang, Longgang Hou, Jinxiang Zhang, Lin Lu, Hua Cui, Jishan Zhang, The secondary precipitates of niobium-alloyed M3:2 high speed steel prepared by spray deposition, Materials Characterization 106 (2015) 245–254.
[29] M. Godec, T. Večko-Pirtovšek, B. Šetina Batič, P. McGuiness, J. Burja, B. Podgornik, Surface and Bulk Carbide Transformations in High-Speed Steel, Scientific Reports, 5 (2015) 1-11.
[30] Wei Shizhong, Zhu Jinhua, Xu Liujie, Long Rui, Effects of carbon on microstructures and properties of high vanadium high-speed steel, Materials and Design 27 (2006) 58–63.
[31] Hwang, K. C., Lee, S. & Lee, H. C. Effects of alloying elements on microstructure and fracture properties of cast high speed steel rolls: Part I: Microstructural analysis, Materials Science & Engineering A 254 (1998), 282–296.

[32] Karagöz, S., Liem, I., Bischoff, E. & Fischmeister, H. F. Determination of carbide and matrix compositions in high-speed steels by analytical electron microscopy, Metallurgical and Materials Transactions A, 20 (1989), 2695–2701.
[33] T. Večko-Pirtovšek, G. Kugler, M. Godec, M. Terčelj, Three important points that relate to improving the hot workability of ledeburitic tool steels, Metallurgical and Materials Transactions A, 43/10 (2012) 3797-808.
[34] C.A.C. Imbert, N.D. Ryan, H.J. McQueen, Hot Workability of Three Grades of Tool Steel, Metallurgical and Materials Transactions A, 15A (1984), 1855-1864.
[35] M. R. Ghomashchi and C. M. Sellars, Microstructural Changes in As-cast M2 Grade during hot Forging Metallurgical and Materials Transactions A, 24A (1993), 2171-2180.
[36] C.A.C. Imbert, H.J. McQueen, Hot ductility of tool steels, Canadian Metallurgical Quarterly 40 (2001) 235-244.
[37] T. Večko-Pirtovšek, G. Kugler, M. Godec, M. Terčelj, Microstructural characterization during the hot deformation of 1.17C–11.3Cr–1.48V–2.24W–1.35Mo ledeburitic tool steel, Materials Characterization, 62 (2011), 189-197.
[38] T. Večko-Pirtovšek, G. Kugler, M. Terčelj, The behaviour of the carbides of ledeburitic AISI D2 tool steel during multiple hot deformation cycles, Materials Characterization 83 (2013) 97-108.
[39] M. Spittel, C. Weiß, T. Spittel, The Influence of Chemical Composition and Deformation Conditions on the Hot-Forming Property of the High-Speed Steel Grades S 6-5-2 and S 6-5-2-5, Neue Hütte, 36 (1991), 284-289.
[40] J. Liu, H. Chang, R. Wu, T.Y. Hsu, X. Ruan, Investigation on hot deformation behaviour of AISI T1 high-speed steel, Materials Characterization 45 (2000) 175-186.
[41] R. Milovic, D. Manojlovic, M. Andjelic and D. Drobnjak, Hot workability of M2 type High-speed steel, Steel Research 63 (1992) 78-84.
[42] C. Rodenburg, M. Kryzanowski, J.H. Beynon, W.M. Rainforth, Hot workability of spray-formed AISI M3:2 high speed steel, Materials Science and Engineering A386 (2004) 420-427.
[43] A. Akbarzadeh, S. Naghdy, Hot workability of a high carbon high chromium tool steel, Materials & Design, 46 (2013) 654-659.
[44] J.J. Jonas, C.M. Sellars, W.J. M. Tegart, Strength and structure under hot working conditions, Metall. Rev., 130 (1969) 1-24.
[45] G. Kugler, M. Knap, H. Palkowski, R. Turk, Estimation of activation energy for calculating the hot workability properties of metals, Metalurgija, 43/4 (2004) 267-272.
[46] D. Bombac, M. Brojan, M. Tercelj, R. Turk, Response to hot deformation conditions and microstructure development of Nimonic 80A superalloy, Materials and Manufacturing Processes, 24 (2009), 644-648.